Materials Advances



PAPER View Article Online



Cite this: *Mater. Adv.*, 2025, 6, 839

DOI: 10.1039/d4ma01000k

Received 5th October 2024, Accepted 16th December 2024

rsc.li/materials-advances

Smart early diagnosis of acute myocardial infarction: a ZIF-based nanofluorescence lateral flow immunoassay for point-of-care detection of cTnI[†]

Zahra Mirzaeizadeh,^a Emadoddin Amin Sadrabadi,^a Neda Naseri,^a Hamed Golmohammadi*^b and Kobra Omidfar (D)*^{ac}

Despite significant progress in the diagnosis of acute myocardial infarction (AMI), its morbidity and mortality rates are still high, indicating the necessity of developing easy-to-use diagnostic tests with timely and reliable point-of-care (POC) detection capability. Aiming to address this need, we introduce here for the first time the development of a fluorescence lateral flow immunoassay (LFIA) based on antibody labeled ZIF-8@BSA Au/Ag nanoclusters for the quantitative detection of cardiac troponin I (cTnI) as the major biomarker of AMI. A portable IoT-enabled optoelectronic reader was also fabricated to quantify the fluorescence signals of the developed LFIA, enabling easy, precise, and smart on-site quantitative analysis of cTnI. The developed smart LFIA demonstrated desirable assay performance for cTn1 in a linear concentration range of 10 pg mL⁻¹ to 150 pg mL⁻¹ with an appropriate sensitivity (with a detection limit of 9 pg mL⁻¹) compared to the enzyme-linked immunosorbent assay (ELISA) and other reported assays. The fascinating results of our developed smart LFIA for easy, rapid (~10 min), and highly sensitive and specific detection of cTnI in serum and whole blood samples make it a very promising biosensor capable of being exploited for smart, reliable, and early diagnosis of AMI at the POC.

Introduction

Acute myocardial infarction (AMI) is one of the primary causes of morbidity and mortality related to cardiovascular diseases (CVDs), and therefore its rapid and accurate diagnosis is crucial for early interventional treatment and improvement of prognosis. Several biomarkers are utilized for the diagnosis of AMI, including cardiac troponin I (cTnI), cardiac troponin T (cTnT), C-reactive protein (CRP), myoglobin, B-type natriuretic peptide (BNP), and creatine kinase isoenzyme MB (CK-MB). Among them, according to the American College of Cardiology guidelines, cTnI is considered the gold standard biochemical marker for early diagnosis of AMI in clinical practices on account of its

high specificity for myocardial damage. It starts to increase within 2-4 h after the onset of symptoms, reaches a maximum at 24-48 h, and maintains a high level for up to 12 days. The significant range of cTnI in the blood is around 0.001-0.1 ng mL⁻¹. In healthy individuals, its levels are in the range of ≤ 0.04 ng mL⁻¹, and levels around 0.1 ng mL-1 indicate damage to cardiac myocytes. 4-6 Conventional analytical methods for cTnI detection include radioimmunoassay, electrochemiluminescence immunoassay, and enzyme-linked immunosorbent assay (ELISA). Nonetheless, these methods are associated with high costs, long testing times, and the need for sophisticated equipment and operators. For these reasons, as well as due to inadequate infrastructure facilities, they are often not available in constrained settings.1,7,8 Therefore, the development of affordable, accurate, rapid, and easy-to-use sensing tools that can be utilized by considering the time-critical nature of cTnI detection for its highly sensitive yet reliable determination in point-of-care (POC) settings is still an important unmet demand. Lateral flow immunoassays (LFIAs) are among the simplest, fastest, and cheapest paper-based POC assays designed to perform diagnostics at the time and place of patient care. There is no need for multiple steps of liquid addition, incubation, washing, and complex detection instruments as well

^a Biosensor Research Center, Endocrinology and Metabolism Molecular–Cellular Sciences Institute, Tehran University of Medical Sciences, P.O. Box 14395/1179, Tehran, Iran. E-mail: omidfar@tums.ac.ir

b Nanosensor Bioplatforms Laboratory, Chemistry and Chemical Engineering Research Center of Iran, Tehran 14335-186, Iran. E-mail: golmohammadi@ccerci.ac.ir

^c Endocrinology and Metabolism Research Center, Endocrinology and Metabolism Research Institute, Tehran University of Medical Sciences, Tehran, Iran

[†] Electronic supplementary information (ESI) available. See DOI: https://doi.org/ 10.1039/d4ma01000k

Paper

as professional operators, making them suitable for field use compared to conventional laboratory methods. 9-13

They can recognize target biochemical markers with an immunecomplex format, similar to the sandwich immunoassay format. However, for most types of LFIAs, the sensitivity is not good enough to detect very low levels of cardiac biomarkers. 14,15 Currently, a variety of fluorescent nanostructures with remarkable luminescence and light conversion characteristics have been produced for use as labels in LFIAs. They are sensitive, stable, and easy to quantify, gradually replacing traditional gold nanoparticles (AuNPs) and becoming one of the most popular signal elements for the quantitative detection of target molecules in LFIAs. 16-22

So far, numerous signal elements have been applied to improve the analytical performance of LFIAs for AMI diagnosis, including quantum dot (QD) NPs, 23 up-conversion materials, 24,25 surface-enhanced Raman scattering (SERS) nanotags, 2,26 europium NPs¹² and also composite NPs such as QD SiO₂^{27,28} and QD/metal-organic frameworks (MOFs). 18 Despite the high sensitivity and quantitative capabilities of these LFIAs, they pose challenges in resource-limited settings, as they require skilled personnel to conduct additional procedures, such as external mixing of samples with nanotags, performing chemical reactions on the membrane, or executing washing steps. Additionally, these techniques usually take tens of minutes to attain results, whereas the time of diagnosis is vital for patients with AMI. In the case of europium NPs as a lanthanide ion, their fluorescence sensitivity is typically higher than that of other nanofluorescent labels; however, the excitation process efficiency is limited by their weak absorption cross-sections, due to parity-forbidden transitions.²⁹ This challenge is often addressed through energy transfer from sensitizer ions, 30 ligands, 31 and host matrix 32 or by coupling with plasmonic nanostructures.²⁹

Metal nanoclusters (NCs) as a new class of fluorophores are formed by a few to hundreds of metal atoms with sizes ranging from sub-nanometer to 2 nm. Among them, the use of noble metal NCs as ideal fluorescent signal elements for substance detection has attracted considerable attention due to their unique characteristics, including ultra-small size, a large proportion of surface atoms, water solubility, excellent stability, good biocompatibility, and strong chemical and fluorescence properties.³³ Recent studies have proven that bimetallic NCs with controlled atomic distributions exhibit extra benefits over single-component systems. The interactions between constituent atoms in bimetallic nanoclusters can alter the electronic and surface structures and consequently increase their chemical and optical characteristics.34-36 Compared with other metals, the addition of silver (Ag) into AuNCs results in a much higher fluorescence intensity than that of individual metal NCs, which is due to the synergetic interactions of Au and Ag on the same platform.36-38 For example, Pan et al. have developed a dualmodel colorimetric/fluorescent LFIA based on glutathionecapped Au/AgNCs and polyethyleneimine-modified AuNPs as a signal probe for rapid and ultrasensitive detection of dicofol with a limit of detection (LOD) of 1.59 ng mL⁻¹.39 Fereja et al. have also introduced red-emitting fluorescent bovine serum albumin

(BSA)-capped Au/AgNCs for the determination of folic acid.³⁶ Although there are some other types of photoluminescent NPs such as europium NPs with higher quantum yields and sensitivity and longer fluorescence lifetimes compared to Ag/Au NCs, higher tunable optical properties, easier surface functionalization, broader excitation spectrum, higher environmental stability, and lower toxicity of Ag/Au NCs make them one of the ideal photoluminescent NPs with fascinating physicochemical features in LFIA applications.

To date, various materials such as SiO₂, polymers, and MOFs have been utilized to load NCs or NPs, leading to the fabrication of novel composites with better biocompatibility and waterdispersibility, yet low toxicity. 17,40,41 MOFs have emerged as significant crystalline porous materials, garnering considerable interest in sensor design due to their unique ability to enhance the sensitivity and robustness of assays. 42,43 Among the various MOFs studied, zeolitic imidazole framework-8 (ZIF-8) was chosen for its advantageous characteristics. ZIF-8 is recognized for its porous structure and high surface area, which enable effective encapsulation of nanostructures. This feature is essential as it increases the loading capacity for molecular targets, thereby improving sensitivity and lowering detection limits in various assays. Furthermore, ZIF-8 can be synthesized efficiently from stoichiometric precursors in an aqueous solution at room temperature, without the need for additional additives. This synthesis process is relatively straightforward compared to the more complex formation of silica-based materials, such as SiO2, which requires specific environmental conditions and non-equilibrium processes, despite the simplicity of the underlying chemical reactions. 44-47

Chi et al. developed a sensitive colorimetric sensor for glucose detection based on glucose oxidase (GOx) and AuNCs co-encapsulated ZIF-8.40 They obtained a 19.3-fold increase in the catalytic activity of the GOx&AuNCs@ZIF-8 compared to the free GOx/AuNC solution. A zirconium metal-organic framework (ZrMOF)@CdTe QDs-based LFIA was also developed by Zou et al. for the qualitative analysis of early AMI biomarkers including heart-type fatty acid binding protein (h-FABP) and cTnT with a LOD of 1 μ g L⁻¹.¹⁸

In the present study, for the first time, by benefiting from the encapsulation of BSA Au/AgNCs within the nanoscaffold of ZIF-8 for improving their stability and emission intensity, we introduce a novel and rapid LFIA for the early quantitative detection of cTnI at the trace levels. In addition, we have fabricated a handheld IoT-enabled optoelectronic reader to quantify the developed LFIA's fluorescence signals, enabling smart, precise, affordable, and easy quantitative detection of cTnI and consequently early diagnosis of AMI at the POC. We have also validated the applicability of our developed smart LFIA for on-site monitoring through highly sensitive and specific detection of cTnI in serum and whole blood samples.

Experimental

Materials and reagents

Nitrocellulose (NC), conjugate pad, sample pad, and absorbent pad were purchased from Millipore. Zinc nitrate hexahydrate (Zn(NO₃)₂·6H₂O), 2-methylimidazole (2-MIM), and sodium hydroxide (NaOH) were purchased from J&K Scientific Ltd. Monoclonal anti-cardiac troponine I antibody, polyclonal anticardiac troponine I antibody, bovine serum albumin (BSA), chloroauric acid (HAuCl₄), 1-ethyl-3-(3-dimethylaminopropyl)carbodiimide (EDC), *N*-hydroxysuccinimide (NHS), and silver nitrate (AgNO₃) were purchased from Sigma Aldrich (Darmstadt, Germany). Deionized (DI) water was used in all the experiments.

Instrumentation

Materials Advances

The fluorescence spectra were recorded using a commercial F-7000 spectrofluorometer (Hitachi, Japan). UV-vis absorption spectra were recorded using a UV-1800 spectrometer (Shimadzu, Japan). Dynamic light scattering (DLS) and zeta potentials were determined using a Nano ZS90 (Malvern, UK). High-resolution transmission electron microscopy (HRTEM) images were obtained with a transmission electron microscope at an accelerating voltage of 200 kV (HRTEM, Tecnai F20, FEI). X-ray diffraction (XRD) (Bruker/D8 Advance) was used to characterize the crystalline structures of samples. Fourier-transform infrared spectroscopy (FT-IR) spectra were recorded between 4000 and 500 cm⁻¹ using a PerkinElmer Frontier Spectrum instrument.

Synthesis of BSA Au/AgNCs

BSA Au/AgNCs were prepared in an aqueous solution according to a previously reported method with a slight modification. 35,48 HAuCl $_4$ solution (5 mL, 10 mM) and aqueous AgNO $_3$ solution (1.25 mL, 8.6 mM) were first added to the BSA solution (5 mL, 50 mg mL $^{-1}$). After stirring at 40 °C for 2 min, 1 mM NaOH solution (0.5 mL) was dropped into the above solution and reacted at 40 °C for 12 h. After the reaction, the color of the solution changed to yellow, which presented an intense orange fluorescence under a UV lamp. Finally, the mixture was purified by dialysis against DI water through a 3 kDa molecular weight cut-off for 48 h to remove unreacted impurities. The dialyzed product was finally freeze-dried and kept at 4 °C before use.

Synthesis of ZIF-8@BSA Au/AgNCs

BSA Au/AgNCs (1.6 mg) were mixed with 25 mM $\rm Zn(NO_3)_2 \cdot 6H_2O$ (5 mL) and 25 mM 2-MIM (5 mL) for 5 min at room temperature under gentle stirring. The mixture was incubated at room temperature for 12 h and then collected by centrifugation after three times of washing (15 min, 3000 rpm) with DI water. ^{40,41}

Synthesis of ZIF-8@BSA Au/AgNCs-monoclonal antibody (mAb) conjugates

ZIF-8@BSA Au/AgNCs-monoclonal antibody (mAb) conjugates were prepared using the EDC/NHS coupling method. The assynthesized ZIF-8@BSA Au/AgNCs (1 mg) were first dispersed in 2 mL of phosphate buffer (PB) (0.01 mM, pH 7.2) and then added to freshly prepared EDC (10 mg mL $^{-1}$, 50 µL) and NHS (10 mg mL $^{-1}$, 50 µL) for activation. After stirring at 25 °C for 1 h, excess EDC and NHS were removed by centrifugation with PB solution (0.01 mM, pH 7.2). Subsequently, 10 µg of anti-cTnI mAb (1 mg mL $^{-1}$) was added to the activated ZIF-8@BSA

Au/AgNC solution. After gentle shaking at room temperature for 1 h, BSA solution (3% w/v) was added to block the remaining functional groups. Finally, the ZIF-8@BSA Au/AgNCs-mAb conjugates were collected by centrifugation and resuspended in 200 μ L of phosphate-buffered saline (PBS, 0.01 M, pH 7.4, containing 1% BSA (w/v) and 0.05% Tween 20 (v/v)).

LFIA fabrication

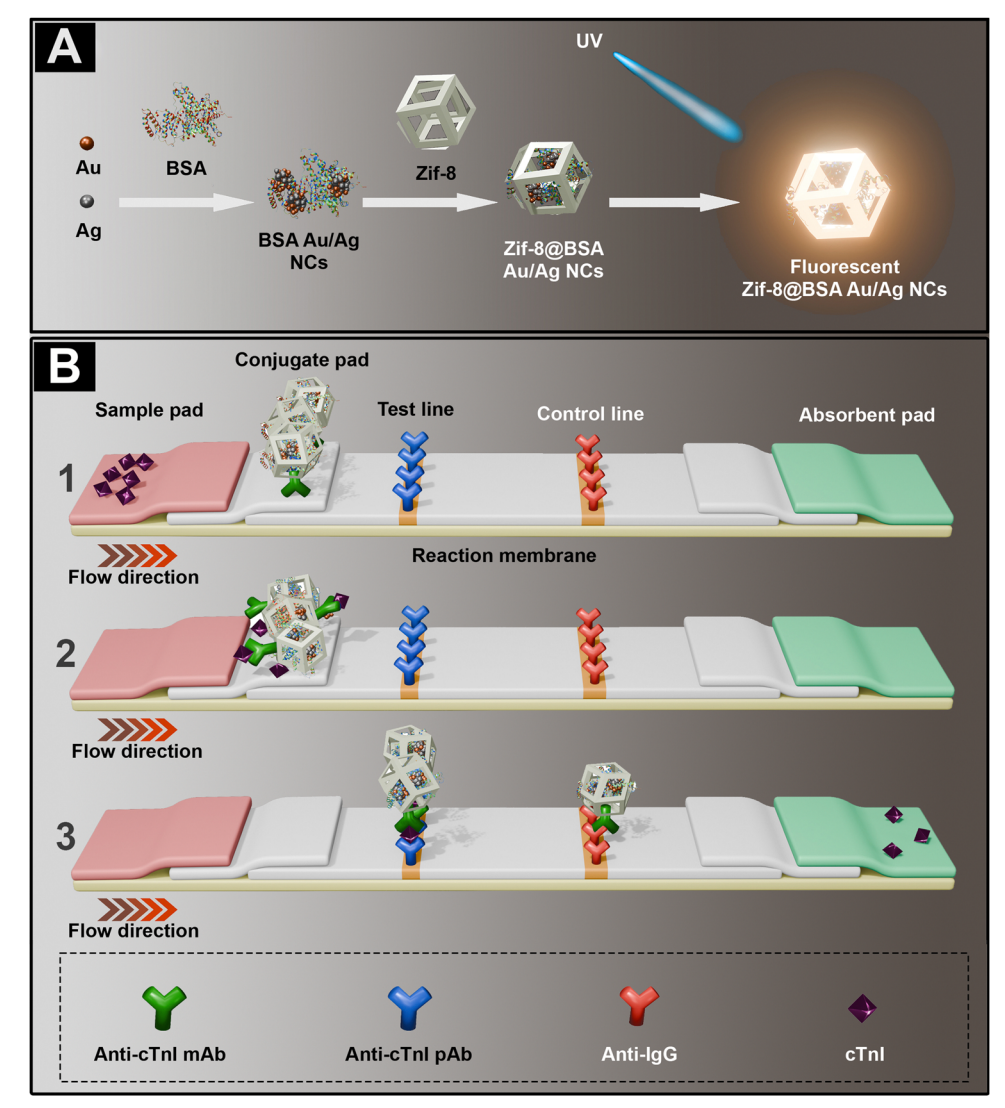
The LFIA strip comprises a sample pad, a conjugate pad, an NC membrane, and an absorbent pad. ⁴⁹ For the LFIA strip assembly, the NC membrane was first immobilized on a supporting laminated card. The solutions of rabbit anti-cTnI capture antibody (0.7 μ g per strip) and anti-mouse IgG (1 μ g per strip) in PBS buffer were separately deposited onto the NC membrane and then dried at 37 °C for 2 h to create the test line (T line) and control line (C line), respectively. The sample pad was first soaked into a PBS solution (0.01 M, pH 7.4, containing 1% BSA, 2% sucrose, and 0.05% Tween 20) and then dried at 37 °C overnight. The sample and absorbent pads were adhered to each end of the backing card, overlapping the NC membrane by 2 mm. The conjugate solution was placed on a glass fiber membrane and dried under vacuum at room temperature for 2 h (Scheme 1). ^{50,51}

Design and fabrication of the smart handheld LFIA reader

The Solidworks 2020 program was used for the design of the smart LFIA reader. A 3D printer (Mark3, Prusa Research, Czech Republic) was used to fabricate the reader's frame/dark chamber, which (as depicted in Scheme 2) has well-defined places for the reader's components (an 11-channel multi-spectral sensor (AS7341, 3.3–5 V, 23 mm \times 30.5 mm, Adafruit, China), a light emitting diode (LED)/emitter 380 nm (model 2835, 3-3.6 V, 0.1 W, China), an IoT-enabled microcontroller unit (MCU) (ESP32, 3.3 V, 28 mm \times 55.3 mm, Arduino, China), an organic light emitting diode (OLED) display (128 \times 64 pixels, 0.96 inch,² 3-5 V, bicolor, Arduino, China), a rechargeable lithium-ion battery 2600 mA h (model 18650, 3.7 V, 65 mm × 18 mm, China), and a charging module (KC 864-2A, 5 V, 5 W, China)). A sample holder was also fabricated using a 3D printer to place the LFA in the reader. After fixing/placing the mentioned segments in their explicit places, the fabricated smart LFIA reader was programmed using Arduino Integrated Development Environment (IDE) software.

Analytical procedure

 $20~\mu L$ of a standard solution containing the corresponding concentration of cTnI or various real samples including human serum, plasma, and blood samples was injected into the sample pad of the fabricated LFIA. Subsequently, $100~\mu L$ of the running buffer (RB) was dropped onto the same pad immediately. The RB contained 0.5% Tween 20 in PBS. 52 In this system, cTnI in the sample or standard solution was attached to the ZIF-8@BSA Au/AgNCs-mAb and then the complexes moved to the NC membrane. The rabbit anti-cTnI polyclonal antibody (pAb) in the T line captured the target complex of ZIF-8@BSA Au/AgNCs-mAb-cTnI, while the excess of the unbound analyte-antibody



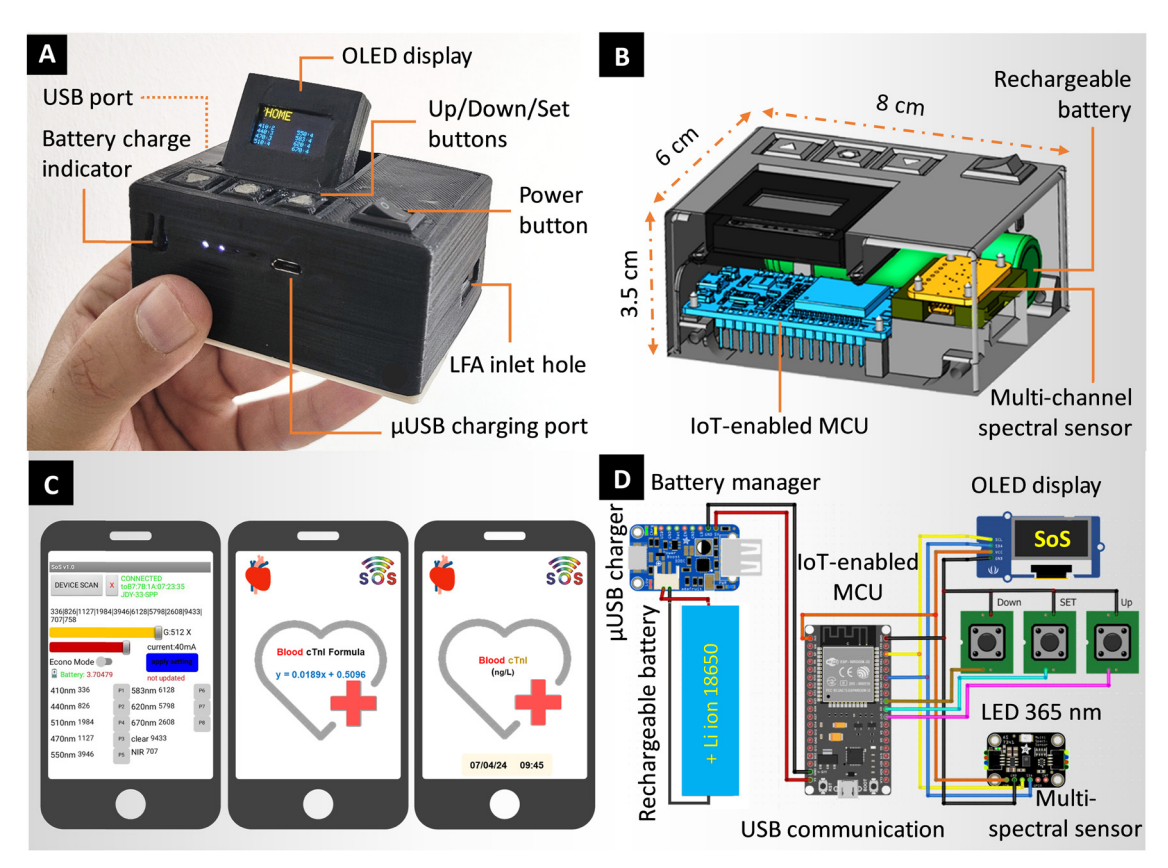
Scheme 1 (A) Schematic representation of ZIF-8@BSA Au/AgNCs. (B) ZIF-8@BSA Au/AgNC nanocomposites based LFIA for the detection of cTnI.

conjugation complex was captured by the secondary antibody in the C line (Scheme 1). After 10 min, the strip was placed inside the fabricated smart reader and subsequently, the fluorescence intensities of the C and T lines of strips in the 600 nm optical channel of the reader were recorded/read. Notably, the fabricated reader was equipped with a 380 nm LED to excite the fluorescence of Au/AgNCs of strips. The signal intensity in the T line was directly proportional to the cTnI level of the sample. The recorded fluorescence signal was then transmitted wirelessly (by the reader IoT module) to a smartphone to quantify the corresponding cTnI concentration (Scheme 2D) using our self-developed smartphone app through the associated calibration equation.

Results and discussion

Considering the crucial role of cTnI detection in the earlier diagnosis and risk assessment of MI and the unmet demand for its reliable sensing at the POC, this study aims to provide an accurate and smart POC LFIA to detect cTnI levels in blood

samples using a sensing platform of MOFs and fluorescent Au/AgNCs, which coupled with a smart portable reader. To the best of our knowledge, this is the first report that has utilized a ZIF-8@BSA Au/AgNC composite as a label in LFIA. The ZIF-8@BSA Au/AgNCs were synthesized by coprecipitating the as-prepared red-emitting fluorescent BSA Au/AgNCs with the ZIF-8 precursors under ambient conditions. The BSA Au/AgNCs, which are negatively charged in an aqueous solution, readily absorbed positively charged Zn2+ ions and then served as the building foundation to fabricate ZIF-8@BSA Au/AgNCs⁴¹ (Scheme 1(A)). The encapsulation of BSA Au/AgNCs into MOFs introduces new characteristics to the MOFs and BSA Au/AgNCs, such as a large surface area, adjustable cavities, photoluminescence capabilities, favorable dispersibility, and biocompatibility. These characteristics can significantly enhance the fluorescence intensity and stability of BSA Au/AgNCs. The use of ZIF-8@BSA Au/AgNCs as fluorescent signal detectors for labeling antibodies, in turn, facilitates the migration of nanotags, enhances visual recognition, reduces misreading errors,



Scheme 2 (A) and (B) Image of the fabricated smart handheld LFIA reader and its components. (C) Images of the self-developed mobile app: from left to right, the spectral data of the fabricated smart LFIA reader in each optical channel and the steps of spectral data formulation in the optical channel of 600 nm to quantify the blood cTnI concentration using the associated calibration equation. (D) Schematic electronic diagram of the fabricated smart LFIA reader.

and ultimately reduces the overall test time required.¹⁸ The monoclonal antibody was covalently conjugated to BSA by crosslinking the carboxyl groups of BSA on the surface of Au/Ag NCs to the amine functional groups of the antibody.

As demonstrated in Scheme 1(B), to perform the LFIA, the liquid sample containing cTnI was dropped onto the sample pad followed by the RF buffer. Then, the mixture solution migrated along with the driven strip through capillary forces and rehydrated the pre-adsorbed ZIF-8@BSA Au/AgNCs-mAb on the conjugate pad to form an immunocomplex with cTnI. When it reached the T line, the immunocomplex was captured by pre-immobilized rabbit anti-cTnI pAb to produce a ZIF-8@BSA Au/AgNCs-mAb-cTnI-pAb sandwich structure via specific antigen-antibody interactions. Whereas excess ZIF-8@ BSA Au/AgNCs-mAb-cTnI further moved to the C line and anchored by pre-immobilized goat anti-mouse IgG to produce another fluorescent band, indicating the validity of the individual test. After the RF buffer solution reached the absorbent pad, the strip was placed inside the fabricated smart reader and then, as described in Section 2.7, the C and T lines' fluorescence intensities in the optical channel (600 nm) of the reader were recorded. The recorded fluorescence signals were then quantified after wireless transmission to a smartphone using a self-developed smartphone app and the corresponding calibration equation (Scheme 2).

Preparation and characterization of nanoparticles

BSA-capped NCs were synthesized using a green and one-step method, employing BSA as both a reducing and a stabilizing agent.²⁹ ZIF-8@BSA Au/AgNCs were prepared by mixing BSA Au/AgNCs, Zn²⁺, and 2-MIM in an aqueous solution at room temperature.

Afterward, the monoclonal antibody was conjugated to the carboxyl group of BSA in the ZIF-8@BSA Au/AgNCs using the EDC/NHS coupling method. The UV-vis absorption and fluorescence emission spectra of ZIF-8@BSA Au/AgNCs are presented in Fig. 1A. Only an absorption peak at 270 nm (Fig. 1A(a)) was observed within the wavelength range of 200-700 nm without any significant surface plasma resonance (SPR) or molecular-like absorption peak.

Upon excitation at 380 nm, a strong emission peak around 600 nm was observed for the ZIF-8@BSA Au/AgNCs, as reported in the literature (Fig. 1A(b) and (c)).36

Additionally, the ZIF-8@BSA Au/AgNCs display a yellow color under visible light, which changes to a red color upon exposure to a 365 nm UV lamp. The size and shape of the ZIF-8 nanostructures and ZIF-8@BSA Au/AgNCs were characterized using field emission scanning electron microscopy (FE-SEM) and high-resolution transmission electron microscopy (HRTEM) (Fig. 1). As shown in Fig. 1(B) and (D), ZIF-8 nanocrystals exhibit a well-spherical shape with an average diameter of 35-45 nm.

Paper

Fluorescence intensity (a.u.) Absorbance (a.u.) 400 500 200 300 600 700

Wavelength (nm)

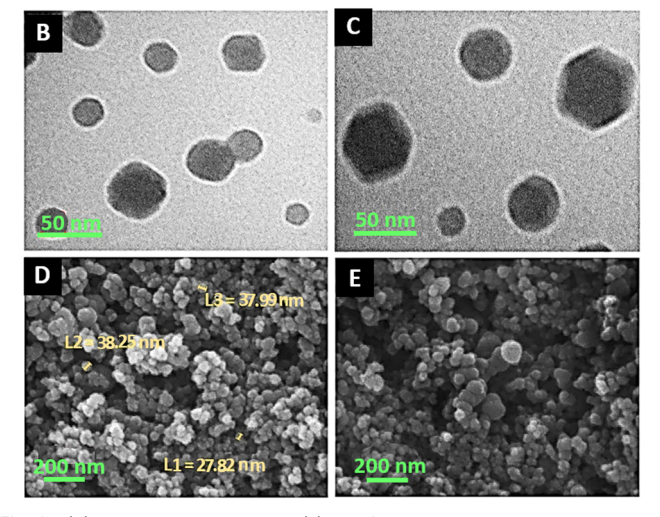


Fig. 1 (A) The UV-vis absorption (a) and fluorescence emission spectra of BSA Au/AgNC (b) and ZIF-8@BSA Au/AgNCs (c) at the same concentration. The excitation wavelength was 380 nm. TEM (B) and SEM (D) images of ZIF-8. TEM (C) and SEM (E) images of ZIF-8@BSA Au/AgNCs.

In addition, from Fig. 1(C) and (E), the ZIF-8@BSA Au/AgNCs have the same structure and size distribution (30-50) as the ZIF-8 nanostructures. The experimental results indicate that when the BSA Au/AgNCs are supported on ZIF-8, there is no noticeable change and aggregation in size and morphology, demonstrating their appropriate stability.^{53,54}

To prove the existence of BSA Au/AgNCs on the surface of ZIF-8 nanostructures, FE-SEM and energy dispersive X-ray spectroscopy (EDS) mapping and analysis were also performed (Fig. 2). The FE-SEM-mapping images (Fig. 2A), as well as the EDS results (Fig. 2B), of ZIF-8@BSA Au/AgNCs clearly confirm that the synthesized ZIF-8@BSA Au/AgNCs are composed of Au, Ag, C, O, N, and Zn. 35,36,41,53,54

Fourier-transform infrared (FTIR) spectroscopy was also utilized to characterize the materials' composition by assessing the vibration frequencies of the functional groups in the spectrum. Additionally, it can be employed to study protein secondary structure changes.

The characteristic IR absorption bands of BSA and BSA Au/ AgNCs are shown in Fig. 2C curves a and b. It can be seen that both O-H and N-H stretching vibrations produce a sharp peak at 3453 cm⁻¹ and 3065 cm⁻¹, respectively. The peak near 1650 cm⁻¹ is attributed to the amide I mode, while the band at 1540 cm⁻¹ is ascribed to the amide II vibration. Even though the FTIR spectra of BSA and BSA Au/AgNCs were highly similar, there are two important differences between them. Fig. 2C curve b displays a shift from 1650 cm⁻¹ to 1640 cm⁻¹ and a slight shift from 1530 cm⁻¹ to 1542 cm⁻¹, indicating the secondary structure modification of BSA after cluster formation and further proving the loading of BSA onto the surface of Au/ Ag NCs. 36,48,55 FTIR spectra were also employed to investigate the structural properties of ZIF-8 and ZIF-8@BSA Au/AgNCs. As depicted in Fig. 2C curves c and d, the spectrum of ZIF-8@ BSA Au/AgNCs is nearly identical to that of ZIF-8. The absorption peaks at 3135 cm⁻¹ and 2929 cm⁻¹ are related to the stretching mode of aliphatic and aromatic C-H of the imidazole in the ZIF-8 nanostructure, respectively. The absorption band at 1579 cm $^{-1}$ is associated with the C=N stretching mode. The absorption band at 420 cm⁻¹ indicates the stretching of the Zn-N bond, while sharp peaks around 1100-1400 cm⁻¹ are assigned to the C-N bending vibration. The characteristic bands of the in-plane and out-of-plane imidazole ring bending are at 692-758 and 952-1178 cm⁻¹, respectively. 53,54

Optimization of key parameters in LFIA

To improve the detection sensitivity and optimize the LFA performance, two important experimental parameters, including the usage amounts of immobilized capture molecule and reporter element, were investigated. The test strips were analyzed in the presence of target cTnI, and the results were evaluated by a smart reader and the naked eve.

Optimization of the immobilized capture rabbit anti-cTnI pAb

The concentration of anti-human cTnI pAb captured at the T line, which directly interacts with ZIF-8@BSA Au/AgNCs-mAbcTnI, is an essential element affecting the sensitivity of LFIA. For this aim, different amounts of capture antibody (0.4, 0.6, 0.7, 0.8, and 0.9 μg per strip) were investigated. The fluorescence signal in the test line is increased by enhancing the concentration of the capture antibodies and reaches a plateau at 0.9 µg per strip (Fig. S1A, ESI†).

Optimization of the volume of ZIF-8@BSA Au/AgNCs-mAb for the conjugate pad

Different amounts (2, 4, 6, and 8 µL per strip) of ZIF-8@BSA Au/AgNCs-mAb were employed to prepare the conjugate pad and used in the LFIA test strip. The results demonstrate that increasing the amount of ZIF-8@BSA Au/AgNCs-mAb leads to an enhancement in the fluorescence signal intensity; however, due to the low fluorescence intensity variation between 6 and 8 μL per strip, 6 μL per strip was chosen as the optimal amount for this assay (Fig. S1B, ESI†).

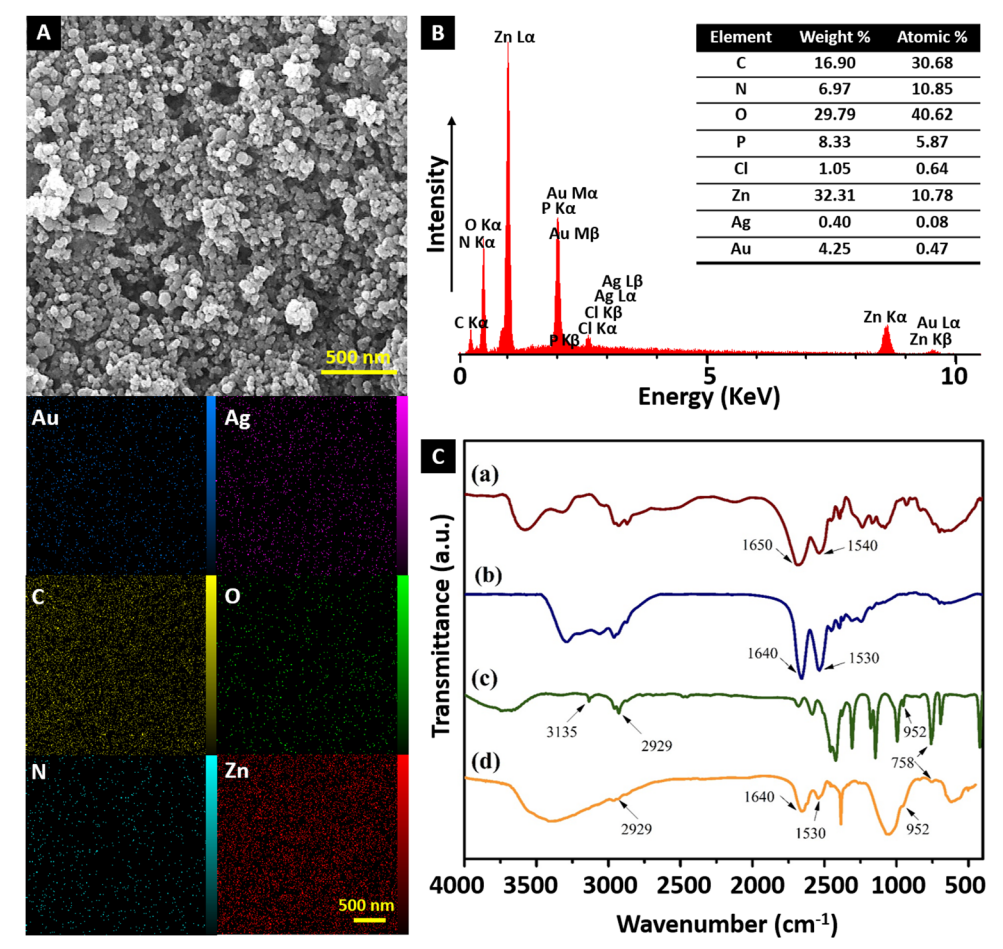


Fig. 2 SEM-EDS surface mapping of ZIF-8@BSA Au/AgNC nanocomposites. (A) FE-SEM image of ZIF-8@BSA Au/AgNCs. Corresponding elemental mapping of Zn, N, Au, and Ag. (B) EDS spectrum of ZIF-8@BSA Au/AgNCs (inset shows the elemental composition). (C) FT-IR spectra of BSA (a), BSA Au/AgNCs (b), ZIF-8 (c), and ZIF-8@BSA Au/AgNCs (d).

Assay performance for the quantitative determination of cTnI

The standard solutions were prepared by dissolving various concentrations of cTnI ranging from 0 pg mL⁻¹ to 300 pg mL⁻¹ with normal serum samples. The fluorescence signal intensity ratios of the T and C lines (FI_T/FI_C) were recorded in triplicate for each concentration of cTnI using the fabricated smart LFIA reader. As shown in the photographs (under UV light) of the fabricated LFIAs in Fig. 3A, the fluorescence intensity at the control line is decreased by increasing the concentration of analyte in the standard samples, indicating all the standard samples have provided valid results for the visible control lines. The FI_T/FI_C ratio is accordingly enhanced with increasing cTnI concentration, which could be employed for detecting cTnI levels in the range of 10-300 pg mL⁻¹ (Fig. 3B). Additionally, the plotted standard curve displayed a good regression coefficient ($R^2 = 0.9995$) between the values of T/C and cTnI concentration from 10 to 150 pg mL⁻¹ (Fig. 3C). The detection limit of the assay was 9 pg mL⁻¹, meeting the clinical diagnostic requirements. To evaluate the repeatability and reproducibility of the assay, the intra-assay and inter-assay were performed using three different concentrations of cTnI, including 10 pg mL⁻¹, 80 pg mL⁻¹, and 150 pg mL⁻¹. The intra-assay coefficient of variation (CV) of the fabricated LFIA was determined by recording the FI_T/FI_C of three different concentration levels of cTnI five times at the same strip. As presented in Table S1 (ESI†), the intra-assay and inter-assay CVs were less than 3.7% and 4.9%, respectively, revealing high repeatability and reproducibility of the developed LFIA. Compared to the existing assays for cTnI analysis, the presented method offers higher sensitivity with a relatively shorter detection time, which can be attributed to the use of ZIF-8@BSA Au/AgNCs-mAb and the smart LFIA reader (Table 1).

Specificity experiment

To evaluate the specificity of the current LFIA, we conducted tests using different proteins, including cTnI, human serum albumin (HSA), hemoglobin (Hb), C-reactive protein (CRP), cTnC, and cTnT, individually on the strip. As demonstrated in Fig. 3D by replacing cTnI with interfering components, only weak signals were recorded, indicating high specificity of the current LFIA for detecting cTnI in clinical samples.

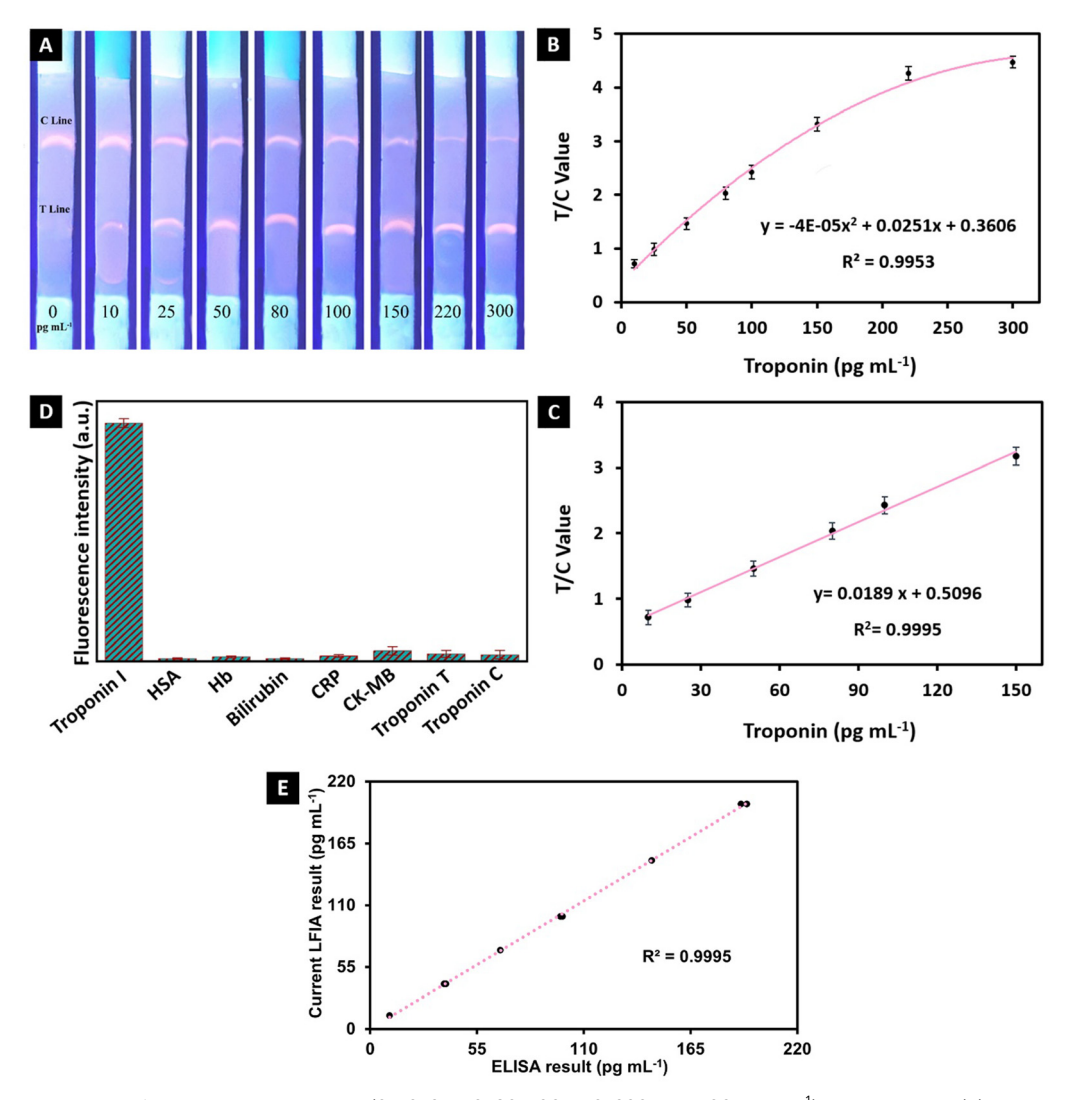


Fig. 3 (A) Qualitative analysis of the cTnl concentrations (0, 10, 25, 50, 80, 100, 150, 220, and 300 pg mL⁻¹) under UV light. (B) The relationship between the fluorescence signal and cTnI concentration from 10 to 300 pg mL⁻¹. (C) The linear calibration plot for cTnI detection with a concentration range of 10-150 pg mL⁻¹. (D) Specificity of the ZIF-8@BSA Au/AgNC based LFIA. The concentrations of HSA, Hb, CRP, CTnT, and cTnC were 20 ng mL⁻¹, 20 ng mL $^{-1}$, 10 ng mL $^{-1}$, 10 ng mL $^{-1}$, and 10 ng mL $^{-1}$, respectively, while the cTnl concentration was 0.1 ng mL $^{-1}$. (E) Correlation analysis of the detectable concentration between smart LFIA and ELISA in nine blood and serum samples with cTnI concentrations from 12 to 200 pg mL⁻¹.

Table 1 Summary of the analytical performances of various LFIA methods for cTnI detection

Method	Sensing probe	Linear range (pg mL ⁻¹)	$LOD (pg mL^{-1})$	Ref.
Chemiluminescent LFIA	PEGYlation of AuNPs	1-90	10	3
LFIA	Europium NPs	0-250	1	12
SERS-based LFA	AuNPs	0.01-100	20	2
Fluorescence LFIA	Fluorescent nanoprobes	0-50	49	56
Fluorescence LFIA	Fluorescent nanoprobes	0-30	32	57
Fluorescence LFIA	ZIF-8@BSA Au/AgNCs	10-150	9	Current

Stability experiment

The stability of the fabricated LFIA was also investigated. Different test strips were provided under the same conditions as elucidated in the Experimental sections and then stored for 14 weeks at 4 °C. Compared to the initial fluorescence signal, no obvious change in the fluorescence signal was recorded (Fig. S2, ESI†).58

Detection of cTnI in real samples

The clinical applicability of the developed smart LFIA was investigated by performing tests on nine serum and whole blood samples and subsequently comparing those results with values obtained using standard ELISA tests (Monobind Inc). The calculated relative standard deviations

Table 2 Comparison of cTnI concentrations in serum and whole blood samples measured by the current smart LFIA and ELISA

Sample	ELISA results (pg mL ⁻¹)	Current LFIA results $(pg mL^{-1})$	RSD (%)
Serum	10	12	2.25
Serum	38	40	3.6
Serum	67	70	3.09
Serum	99	100	0.7
Serum	191	200	3.2
Blood	39	40	5.5
Blood	98	100	1.4
Blood	145	150	2.37
Blood	194	200	2.15

(RSDs) from three repeated analyses for patient and control samples are shown in Table 2. The obtained RSDs (0.7–3.61%), as well as good correlation ($R^2 = 0.9995$) between the results of the developed smart LFIA and ELISA (Fig. 3E), confirm that the presented method is capable of detecting cTnI in real clinical samples.

Conclusions

In summary, we have successfully established a sensitive, simple, and quantitative LFIA based on the combination of a double-signal amplification strategy for early and rapid diagnosis of AMI. First, due to the encapsulation of a large number of negatively charged BSA Au/AgNCs within ZIF-8, the fluorescence signal has been strongly amplified, resulting in a rich signal-to-noise ratio throughout the analysis procedure. Second, the use of a portable IoT-enabled optoelectronic reader enables smart, reliable, yet simple on-site quantitative analysis of cTnI. The LoD of the assay for cTnI was 0.009 ng mL⁻¹, which is lower than the present AMI detection standard (0.04 ng mL⁻¹). Moreover, the fabricated LFIA has an appropriate linear range, acceptable specificity, reproducibility, and long-term stability. Building upon the fascinating results of our developed smart LFIA for easy, highly sensitive, specific, and rapid (~10 min) cTnI detection in serum and whole blood samples, we believe it would be a promising biosensor capable of being utilized for early, reliable, and smart POC diagnosis of AMI.

Author contributions

K. O.: conceptualization, methodology, resources, supervision, investigation, original paper writing, review, and editing. Z. M.: investigation, formal analysis, and visualization. H. G.: supervision, resources, investigation, writing, review, and editing. E. M.: formal analysis and visualization. N. N.: formal analysis and visualization. All authors have approved the final version of the manuscript.

Data availability

The authors confirm that the data supporting the findings of this study are available within the article and its ESI. \dagger

Conflicts of interest

The authors declare no competing financial interest.

Acknowledgements

This study was supported by a grant from the Endocrinology and Metabolism Research Institute of Tehran University of Medical Sciences in Iran. The authors acknowledge financial support from the Endocrinology and Metabolism Research Institute of Tehran University of Medical Sciences and the Chemistry & Chemical Engineering Research Centre of Iran (Tehran, Iran).

References

- 1 A. Ahmadi, S. M. Khoshfetrat, Z. Mirzaeizadeh, S. Kabiri, J. Rezaie and K. Omidfar, *Talanta*, 2021, 237, 122911.
- 2 E. Song, I. Kim, C. Jeon and S. Pyun, *Microchem. J.*, 2023, 193, 108962.
- 3 Z. Ren, L. Xu, L. Yang and Y. Cui, *Anal. Chem.*, 2023, **95**, 6646–6654.
- 4 R. D. Crapnell, N. C. Dempsey, E. Sigley, A. Tridente and C. E. Banks, *Mikrochim. Acta*, 2022, **189**, 142.
- 5 S. Norouzi Eshlaghi, L. Syedmoradi, A. Amini and K. Omidfar, IEEE Sens. J., 2023, 1.
- 6 X. Chen, C. Zhang, X. Liu, Y. Dong, H. Meng, X. Qin, Z. Jiang and X. Wei, *Microsyst. Nanoeng.*, 2023, 9, 141.
- 7 J. Chen, X. Sun, Y. Wang, Z. Gao and B. Zheng, *Sens. Actuators*, *B*, 2023, **385**, 133712.
- 8 X. Han, S. Li, Z. Peng, A. M. Othman and R. Leblanc, *ACS Sens.*, 2016, 1, 106–114.
- 9 S. Schuster da Silva, M. L. Cunha, L. B. Ayres, C. D. Garcia and L. Blanes, *Anal. Methods*, 2023, **15**, 3610–3630.
- 10 R. Agarwal, S. O. Martinez-Chapa and M. J. Madou, *Sci. Rep.*, 2023, **13**, 18296.
- 11 N. Poosinuntakul, T. Chanmee, S. Porntadavity, O. Chailapakul and A. Apilux, *Sci. Rep.*, 2022, 12, 19866.
- 12 S. Natarajan and J. Joseph, Science Talks, 2023, 5, 100151.
- 13 X. Ying, W. Fu, L. Zhu, T. Sun, M. Qi, L. Zhou, Y. Wang, J. Wang, B. Su and J. Zhang, *Anal. Chem.*, 2024, 96, 10630–10638.
- 14 K. Omidfar, F. Riahi and S. Kashanian, *Biosensors*, 2023, 13, 837.
- 15 Y. Liu, L. Zhan, Z. Qin, J. Sackrison and J. C. Bischof, ACS Nano, 2021, 15, 3593–3611.
- 16 B. Liu, J. Li, X. Tang, Z. Wu, J. Lu, C. Liang, S. Hou, L. Zhang, T. Li, W. Zhao, Y. Fu, Y. Ke and C. Li, Development of a quantum-dot lateral flow immunoassay strip based portable fluorescence smart-phone system for ultrasensitive detection of IgM/IgG to SARS-CoV-2, 2020.
- 17 L. Huang, T. Liao, J. Wang, L. Ao, w su and J. Hu, *Adv. Funct. Mater.*, 2018, **28**, 1705380.
- 18 J. Zou, X. Liu, X. Ren, L. Tan, C. Fu, Q. Wu, Z. Huang and X. Meng, *Nanoscale*, 2021, **13**, 7844–7850.

Paper

19 A. Sena, H. Torné-Morató, C. Parolo, S. Ranjbar, M. A. Farahmand Nejad, R. Alvarez Diduk, A. Idili, M. R. Hormozi-Nezhad and A. Merkoçi, Adv. Mater. Technol., 2022, 7.

- 20 S. K. Kim, H. Sung, S. H. Hwang and M. N. Kim, BioChip J., 2022, 16, 175-182.
- 21 P. Zheng, T. Peng, J. Wang, J. Zhang, Z. Wang, Y. Zhang, Z. Ren, S. Wang and H. Jiang, Microchim. Acta, 2021,
- 22 J. Wang, C. Jiang, J. Jin, L. Huang, W. Yu, B. Su and J. Hu, Angew. Chem., Int. Ed., 2021, 60, 13042-13049.
- 23 M. Savin, C. M. Mihailescu, I. Matei, D. Stan, C. A. Moldovan, M. Ion and I. Baciu, Talanta, 2018, 178, 910-915.
- 24 Y. Li and Y. Li, Inorg. Chem., 2024, 63, 5185-5198.
- 25 S. Bayoumy, I. Martiskainen, T. Heikkilä, C. Rautanen, P. Hedberg, H. Hyytiä, S. Wittfooth and K. Pettersson, Sci. Rep., 2021, 11, 18698.
- 26 B. N. Khlebtsov, D. N. Bratashov, N. A. Byzova, B. B. Dzantiev and N. G. Khlebtsov, Nano Res., 2019, 12, 413-420.
- 27 M. Wu, X. Zhang, R. Wu, G. Wang, J. Li, Y. Chai, H. Shen and L. S. Li, Anal. Lett., 2020, 53, 1757-1773.
- 28 J. Li, Y. Lv, N. Li, R. Wu, J. Li, J. You, H. Shen, X. Chen and L. S. Li, Sens. Actuators, B, 2021, 344, 130275.
- 29 L. Bertry, O. Durupthy, P. Aschehoug, B. Viana and C. Chanéac, Gold Bull., 2013, 46, 349-355.
- 30 K. Binnemans, Chem. Rev., 2009, 109, 4283-4374.
- 31 A. Døssing, Eur. J. Inorg. Chem., 2005, 1425-1434.
- 32 A. Huignard, T. Gacoin and J.-p Boilot, Chem. Mater., 2000, 12, 1090-1094.
- 33 L. Chen, M. Gharib, Y. Zeng, S. Roy, C. K. Nandi and I. Chakraborty, Mater. Today Chem., 2023, 29, 101460.
- 34 X. Le Guével, B. Hötzer, G. Jung, K. Hollemeyer, V. Trouillet and M. Schneider, J. Phys. Chem. C, 2011, 115, 10955-10963.
- 35 R. Dai, W. Deng, P. Hu, C. You, L. Yang, X. Jiang, X. Xiong and K. Huang, Microchem. J., 2018, 139, 1-8.
- 36 S. L. Fereja, P. Li, J. Guo, Z. Fang, Z. Zhang, Z. Zhuang, X. Zhang, K. Liu and W. Chen, Talanta, 2021, 233, 122469.
- 37 J. Jana, P. Acharyya, Y. Negishi and T. Pal, ACS Omega, 2018, 3, 3463-3470.
- 38 K. Sahoo, T. R. Gazi, S. Roy and I. Chakraborty, Commun. Chem., 2023, 6, 157.
- 39 Y. Pan, X. Wei, X. Guo, H. Wang, H. Song, C. Pan and N. Xu, Biosens. Bioelectron., 2021, 194, 113611.

- 40 J. Chi, M. Guo, C. Zhang, Y. Zhang, S. Ai, J. Hou, P. Wu and X. Li, New J. Chem., 2020, 44, 13344-13349.
- 41 Y. Sun, T. Shu, J. Ma, Q. Dai, P. Peng, Z. Zhou, X. Zhou, L. Su and X. Zhang, Anal. Chem., 2022, 94, 3408-3417.
- 42 Q. Zhang, S. Yan, X. Yan and Y. Lv, Sci. Total Environ, 2023, 902, 165944.
- 43 L. León-Alcaide, J. López-Cabrelles, M. Esteve-Rochina, E. Ortí, J. Calbo, B. A. H. Huisman, M. Sessolo, J. C. Waerenborgh, B. J. C. Vieira and G. Mínguez Espallargas, J. Am. Chem. Soc., 2023, 145, 23249-23256.
- 44 H. Mei, J. Xie, Z. Li, C. Lou, G. Lei, X. Liu and J. Zhang, CrystEngComm, 2022, 24, 1645-1654.
- 45 H. N. Abdelhamid, Curr. Med. Chem., 2021, 28, 7023-7075.
- 46 Y. Zhao, X.-W. Zhu, W. Lu and D. Li, Chem. Soc. Rev., 2021, 50, 4484-4513.
- 47 A. Zuliani, N. Khiar and C. Carrillo-Carrión, Anal. Bioanal. Chem., 2023, 415, 2005-2023.
- 48 A. Ahmadi, S. M. Khoshfetrat, S. Kabiri, P. S. Dorraji, B. Larijani and K. Omidfar, Microchim. Acta, 2021, 188, 296.
- 49 A. A. Patil, P. Kaushik, R. D. Jain and P. P. Dandekar, ACS Infect. Dis., 2023, 9, 9-22.
- 50 B. Gosselin, M. Retout, I. Jabin and G. Bruylants, Sens. Diagn., 2024, 3, 248-255.
- 51 A. Ahmadi, Z. Mirzaeizadeh and K. Omidfar, Monoclonal Antibodies Immunodiagn. Immunother., 2021, 40, 210-218.
- 52 M. Salvador, J. L. Marqués-Fernández, A. Bunge, J. C. Martínez-García, R. Turcu, D. Peddis, M. d M. García-Suárez, M. D. Cima-Cabal and M. Rivas, Nanomaterials, 2022, 12, 2044.
- 53 S. Sadiq, I. Khan, M. Humayun, P. Wu, A. Khan, S. Khan, A. Khan, S. Khan, A. F. Alanazi and M. Bououdina, ACS Omega, 2023, 8, 49244-49258.
- 54 J. Liu, J. He, L. Wang, R. Li, P. Chen, X. Rao, L. Deng, L. Rong and J. Lei, Sci. Rep., 2016, 6, 23667.
- 55 S. Govindaraju, S. R. Ankireddy, B. Viswanath, J. Kim and K. Yun, Sci. Rep., 2017, 7, 40298.
- 56 D. Lou, L. Fan, Y. Ji, N. Gu and Y. Zhang, Anal. Methods, 2019, 11, 3506-3513.
- 57 D. Lou, L. Fan, Y. Cui, Y. Zhu, N. Gu and Y. Zhang, Anal. Chem., 2018, 90, 6502-6508.
- 58 K. Omidfar, M. J. Rasaee, A. B. Zaraee, M. P. Amir and F. Rahbarizadeh, J. Immunoassay Immunochem., 2002, 23, 385-398.